International Journal of Heat and Mass Transfer 146 (2020) 118883

Contents lists available at ScienceDirect

International Journal of Heat and Mass Transfer

journal homepage: www.elsevier.com/locate/ijhmt

Heat and mass transfer during a sudden loss of vacuum in a liquid helium cooled tube – Part II: Theoretical modeling

Shiran Bao [a], Nathaniel Garceau [a,b], Wei Guo [a,b,*]

[a] National High Magnetic Field Laboratory, 1800 East Paul Dirac Drive, Tallahassee, FL 32310, USA
[b] Mechanical Engineering Department, Florida State University, Tallahassee, FL 32310, USA

ARTICLE INFO

Article history:
Received 12 August 2019
Received in revised form 4 October 2019
Accepted 11 October 2019
Available online 22 October 2019

Keywords:
Gas propagation
Loss of vacuum
Superfluid helium
Cryogenics
Particle accelerator

ABSTRACT

A sudden loss of vacuum in particle accelerator beamlines and other cryogenic systems can lead to substantial equipment damage and possible personnel injuries. Developing a clear understanding of the complex dynamical heat and mass transfer processes involved following a sudden vacuum break is of great importance for the safe operation of these systems. Our past experimental studies on sudden vacuum break in a liquid helium cooled tube revealed a nearly exponential slowing down of the propagating gas front. However, the underlying mechanism of this slowing down is not fully explained. In this paper, we discuss a theoretical framework that systematically describes the gas dynamics, heat transfer, and mass deposition of the propagating and condensing gas inside the helium-cooled tube. The experimentally observed apparent gas-front propagation, measured as the abrupt temperature rise by the thermometers installed along the tube wall, can be well reproduced by the model simulation. We also show that following the gas front, the mass deposition rate of the gas on the tube inner wall approaches a constant. The extension of this nearly constant gas deposition zone is the key to understand the observed exponential slowing of the gas propagation. Our model also allows us to gain valuable insights about the growth of the frost layer on the tube inner surface. This work paves the way for a theoretical understanding of the physical processes involved during vacuum break in accelerator beamlines.

1. Introduction

A sudden catastrophic loss of vacuum is one of the most serious failures in liquid helium (LHe) cooled cryogenic systems, e.g., storage vessels, superconducting magnets, particle accelerators. The design and fabrication process seeks to mitigate the risk of vacuum failure in these systems but the possibility of vacuum loss can not be fully eliminated. Knowledge about the underlying dynamical heat and mass transfer processes are of great importance for the proper design of safety components and to minimize possible damage. The most common concern regarding loss of vacuum is the potential overpressure of the liquid reservoir due to the rapid boiling of the cryogen. This overpressure hazard has been studied experimentally and numerically but more work is needed to understand the gas dynamics and condensation in long tube systems such as particle accelerators [1–4].

A major concern specifically for particle accelerators is the propagation and condensation of air within the system after a vacuum break. Particle accelerators are composed of interconnected superconducting cavity chambers called cryomodules. These linked cryomodules create a vacuum beamline up to several kilometers in length. A vacuum break in one of these cavities could lead to a substantial damage throughout the entire system [5]. Furthermore, considering the high cleanness requirement of superconducting cavities, propagation of air and dust through the cavities can cause the suspension in system operation for extended period of time before it can be thoroughly cleaned. To mitigate these risks, fast-acting valves installed to the beamline's vacuum are generally used to prevent the contamination from spreading to multiple cryomodules [6]. However, very limited work has been conducted in this topic area and there are no universal standards available for the design of vacuum interlock components.

The propagation of air in a room-temperature tube driven by a pressure head, known as the shock tube problem, has been well studied and understood [7]. For the extreme case of a nearly absolute vacuum in the tube, a shock wave front can propagate at a speed close to $2c_0/(\gamma-1)$, where c_0 is the speed of sound and γ is the ratio of the specific heats [8]. However, in a particle accelerator, air rushing into the beamline tube can condense on the cold tube inner surface, which has been shown to drastically slow down the air propagation. A propagation speed around 10 m/s was recorded in multiple vacuum failure studies at accelerator labs,

* Corresponding author at: National High Magnetic Field Laboratory, 1800 East Paul Dirac Drive, Tallahassee, FL 32310, USA.
E-mail address: wguo@magnet.fsu.edu (W. Guo).

https://doi.org/10.1016/j.ijheatmasstransfer.2019.118883
0017-9310/

Nomenclature

B_w	coefficient in the film boiling correlation of He I ($W/(cm^2 \cdot K^{5/4})$)
C	specific heat (J/(kg·K))
C_{eff}	effective sticking efficient
D_1	inner diameter of the tube (m)
D_2	outer diameter of the tube (m)
E	critical energy (J)
h	enthalpy (J/kg)
k	thermal conductivity (W/(m·K))
k_b	Boltzmann constant (J/K)
$\dot{m}_0$	mass collision rate on the wall ($kg/(m^2 \cdot s)$)
$\dot{m}_c$	mass deposition rate ($g/(m^2 \cdot s)$)
$\dot{m}$	mass flow rate (kg/s)
M	gas molar mass (kg/mol)
Nu	Nusselt number
P	pressure (Pa)
P_e	equilibrium pressure (Pa)
P_s	saturation vapor pressure (Pa)
q^*	maximum nucleate boiling heat flux (W/m^2)
q_{con}	conductive heat flux along the wall (W/m^2)
q_{dep}	deposition heat flux (W/m^2)
q_{He}	heat flux to the liquid helium bath (W/m^2)
q_i	heat flux to the inner tube surface (W/m^2)
q_R	minimum film boiling heat flux (W/m^2)
R	ideal gas constant (J/(mol·K))
t	time (s)
T	temperature (K)
T_c	temperature of the SN_2 layer (K)
v	velocity (m/s)
x	axial coordinate (m)

Greeks

α	sticking coefficient
α_s	speed of sound (m/s)
γ	heat capacity ratio
δ	thickness of the SN_2 layer (m)
ΔT_{sw}	temperature difference across the SN_2 layer (K)
ΔT_w	temperature difference for He heat transfer (K)
ε	specific internal energy (J/kg)
ρ	density (kg/m^3)
μ	viscosity (Pa·s)

Subscripts

g	bulk gas condition
s	surface of SN_2 layer
w	copper tube wall
SN	solid nitrogen

which is orders of magnitude smaller than the measured speeds at room temperature (i.e., 630 m/s or greater) [9–12].

Early experiments conducted by Dhuley and Van Sciver in our lab tested pure nitrogen gas propagating in a straight tube immersed in either normal liquid helium (He I) or superfluid helium (He II) [13–15]. Results from these experiments showed an exponential slowing of the gas front propagation and a freeze-out phenomenon at low inlet mass flow rates. A simple model based on mass conservation analysis was utilized by these authors to explain the observed slowing down of the gas propagation. In our recent experiments, an upgraded helical tube system with an insulated inlet section was adopted so that we can accurately control the inlet gas conditions and the location where the gas condensation starts [16,17]. The results of this well-controlled experiment confirmed similar exponential slowing down of the gas propagation and suggested slightly enhanced slowing down in He II cooled tube. However, the underlying physical mechanism that leads to the observed exponential slowing down was not explained.

In this paper, we describe a theoretical model for nitrogen gas (GN_2) propagating in a helium-cooled vacuum tube. This model systematically accounts for the fully-coupled gas flow, heat transfer, and mass deposition processes. We have carried out numerical simulations based on this model to compare with our experimental data for model validation. The experimentally observed gas-front propagation, measured as the abrupt temperature rise by the thermometers installed along the tube wall, can be well reproduced by the model simulation. Valuable insight about the growth of the frost layer on the tube inner surface is also obtained. This work paves the way for a theoretical understanding of the complex physical processes involved in beamline vacuum break, which will benefit the design and safe operation of accelerator beamline cryogenic systems.

2. Theoretical model

In our vacuum break experiments, room temperature GN_2 at a controlled inlet mass flow rate is allowed to flow into an evacuated tube that is housed in a helium cryostat [17]. This tube has an inner diameter of 25.4 mm, a wall thickness 1.25 mm, and a length of 6.45 m. The lower tube section with a length of 5.88 m is made of copper and is immersed in the liquid helium bath. The tube section above the liquid surface is made of stainless steel and is wrapped by a multi-layer insulation (MLI) blanket together with a vacuum jacket. This upper stainless steel section also incorporates a heater with a temperature controller such that its temperature is always maintained at above 77 K. This setup allows us to accurately control the starting point of the GN_2 condensation in the tube and eliminate the influence of helium vapor to the upper tube section. In the initiate state, the tube is evacuated with a turbo pump. At time $t = 0$, a fast-acting solenoid valve (25 ms opening time) that connects between a nitrogen buffer tank and the tube opens to simulate vacuum break in the system. A venturi pipe situated immediately after the solenoid valve chokes the gas flow by limiting the velocity of the gas to the speed of sound at the venturi pipe's throat. The mass flow rate of GN_2 at the inlet of the copper tube can be determined by monitoring the rate of the pressure drop in the nitrogen tank [16]. In order to make direct comparison with our experimental observations, we set the tube dimension and other relevant parameters in our model to match exactly the experimental conditions, as shown in the schematic in Fig. 1. The definitions of all the relevant parameters are provided in the Nomenclature table.

2.1. Gas dynamics

First, one can easily check that the compressibility factor of the GN_2 in our entire experiment is always close to unity. Therefore, we can treat the GN_2 as an ideal gas and describe its state by the ideal gas equation of state $PM_g = \rho_g RT_g$. Then, to describe the dynamical evolution of the GN_2 in the copper tube, we consider the conservation laws of N_2 mass, momentum, and energy as discussed below. Due to the small diameter-to-length ratio of the tube and the fact that the radial heat transfer characteristic time is much smaller than the gas propagation time, we model the gas dynamics in one dimensional (1D) space along the tube.

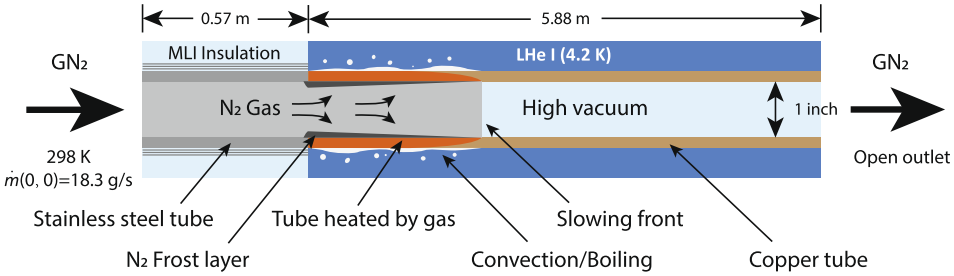

Fig. 1. Schematic showing the propagation and deposition of GN_2 in a He I cooled vacuum tube.

(1) Mass Conservation: The mass conservation equation for the propagating GN_2 can be written as:

$$\frac{\partial \rho_g}{\partial t} + \frac{\partial}{\partial x}(\rho_g v) = -\frac{4}{D_1}\dot{m}_c \tag{1}$$

where the term on the right hand side describes the effect due to N_2 condensation on the tube inner wall. The parameter $\dot{m}_c$ denotes the mass deposition rate of N_2 per unit area, which is expected to depend on local GN_2 conditions and the wall temperature and therefore should vary along the tube. To model $\dot{m}_c$, we introduce an effective sticking coefficient C_{eff} and write $\dot{m}_c = \dot{m}_0 \cdot C_{eff}$, where $\dot{m}_0$ is a normalization factor equaling the rate of mass collision on the wall per unit area for ideal gas:

$$\dot{m}_0 = \frac{1}{4}\sqrt{\frac{8RT_g}{\pi M_g}}\rho_g \tag{2}$$

It has been known in cryopumping research that in the free molecular flow regime, C_{eff} can be modeled as [18–20]:

$$C_{eff} = \left(1 - \frac{P_e}{P}\right)\alpha \tag{3}$$

where $P_e = P_s\sqrt{T_g/T_s}$ denotes the equilibrium pressure, and α is the sticking probability that describes the chance a gas molecule colliding on a cold surface gets stick to it. α depends on the oversaturation ratio (i.e., P/P_e), the gas temperature T_g, and the surface temperature T_s. For nitrogen, α has been measured experimentally at some specific conditions [21,22]. In general, α approaches 1 when $P/P_e \gg 1$ and drops down to a finite value when $P/P_e \to 1$. At $P/P_e < 1$, there is no condensation and simply $C_{eff} = 0$. In Fig. 2, we show the dependance of α on P/P_e and T_s at N_2 gas temperature $T_g = 300$ K, based on the interpolation of experimental data [19].

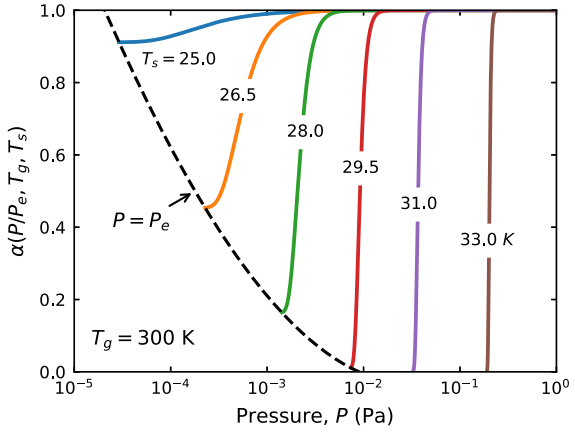

Fig. 2. Sticking probability α of GN_2 at 300 K as a function of gas pressure P at various surface temperature T_s.

The curves for α at other gas temperatures can be obtained by scaling the values shown in Fig. 2 through the relation [22]:

$$\mathrm{Log}(1-\alpha) = -\frac{E}{k_b T_g} \tag{4}$$

where E is the so-called "critical energy" and is a constant for a given surface temperature [22].

We must emphasize that the above-described sticking coefficient model is applicable to the free molecular flow regime. In our experiment, the flow of the GN_2 is essentially in the continuum flow regime. The collisions between gas molecules near the wall can become important and may alter the behavior of C_{eff}. However, due to the limited experimental work and the challenges in evaluating the rate of molecule impingement in the continuum flow regime, there is no reliable existing knowledge about C_{eff} in this regime [23,24]. Nevertheless, we shall show that the above C_{eff} model indeed well accounts for our experimental observations.

(2) Momentum Conservation: The momentum conservation equation for the propagating GN_2 is given by:

$$\frac{\partial}{\partial t}(\rho_g v) + \frac{\partial}{\partial x}(\rho_g v^2) = -\frac{\partial P}{\partial x} - \frac{4}{D_1}\dot{m}_c v \tag{5}$$

where the last term on the right hand side accounts for the momentum loss to the tube wall due to the mass deposition. This equation is essentially the Navier-Stokes equation for compressible fluids with the added term to account for mass deposition effect. The viscous term that usually exists in the Navier-Stokes equation is dropped here since the 1D gas flow in our case is controlled by the inertial effect and the mass deposition.

(3) Energy Conservation: The energy conservation equation for the GN_2 in the copper tube can be derived based on the thermodynamics first law analysis:

$$\begin{aligned}&\tfrac{\partial}{\partial t}\left[\rho_g\left(\varepsilon_g + \tfrac{1}{2}v^2\right)\right] + \tfrac{\partial}{\partial x}\left[\rho_g v\left(\varepsilon_g + \tfrac{1}{2}v^2 + \tfrac{P}{\rho_g}\right)\right] = \\ &-\tfrac{4}{D_1}\dot{m}_c\left(\varepsilon_g + \tfrac{1}{2}v^2 + \tfrac{P}{\rho_g}\right) - \tfrac{4}{D_1^2}Nu\cdot k_g(T_g - T_s)\end{aligned} \tag{6}$$

The two terms on the right hand side account for the loss of energy due to N_2 mass deposition on the tube wall and the convective heat transfer from the gas to the cold SN_2 frost layer. The surface temperature of the frost layer T_s needs to be determined through the radial heat transfer analysis (see discussions below). The Nusselt number Nu for the GN_2 convective heat transfer is evaluated using the Sieder-Tate correlation [25]:

$$Nu = 0.027 Re^{4/5} Pr^{1/3}(\mu_g/\mu_s)^{0.14} \tag{7}$$

2.2. Radial heat transfer

In order to solve the above-mentioned 1D equations for the gas dynamics, we need to analyze the radial heat transfer and determine the frost layer surface temperature T_s. Fig. 3 shows a schematic of the relevant radial heat transfer processes. The heat flux

q_{dep} from the GN_2 to the frost layer consists of contributions from both the energy associated with the deposited molecules (i.e., the kinetic energy, and the sensible and latent heat) and the convective heat transfer:

$$q_{dep} = \dot{m}_c\left[\frac{1}{2}v^2 + h_g - h_s\right] + \frac{Nu \cdot k_g}{D_1}(T_g - T_s) \tag{8}$$

When the frost layer thickness is small, it is reasonable to assume that the temperature profile in the frost layer always takes an equilibrium linear profile. With this simplification, the variation of the frost layer center temperature $T_c = (T_w + T_s)/2$ can be evaluated via:

$$\rho_{SN} C_{SN} \delta \frac{\partial T_c}{\partial t} = q_{dep} - q_i \tag{9}$$

where $q_i = k_{SN}(T_s - T_w)/\delta$ denotes the heat flux into the copper wall. Here we adopt the density ρ_{SN}, specific heat C_{SN}, and thermal conductivity k_{SN} of solid nitrogen at T_c for the frost layer for reasons that will be discussed in detail in Section 3.3. The frost layer thickness δ grows with time and is given by:

$$\frac{\partial \delta}{\partial t} = \dot{m}_c/\rho_{SN}. \tag{10}$$

The evolution of the copper tube wall temperature T_w, which is also required for solving Eq. 9, is governed by:

$$\rho_w C_w \frac{D_2^2 - D_1^2}{4D_1}\frac{\partial T_w}{\partial t} = q_i - q_{He}\frac{D_2}{D_1} + \frac{D_2^2 - D_1^2}{4D_1}k_w\frac{\partial^2 T_w}{\partial x^2} \tag{11}$$

where q_{He} is the heat flux into the He I bath. Due to the high thermal conductivity of copper and the small wall thickness, the copper wall is treated as a lumped-heat-capacity system with a nearly uniform temperature T_w through the wall thickness.

The heat transfer into the He I bath with a time-varying heat flux q_{He} is a complicated transient process that has not been thoroughly studied. Nevertheless, the onset time of film boiling in He I at high heat fluxes (i.e., $>2\ W/cm^2$) is generally at the sub-millisecond scale [26]. Therefore, it is reasonable to adopt the heat transfer correlations for steady-state heat transfer in He I, as depicted in Fig. 4. When the temperature difference ΔT_w between the tube wall and the He I bath is small (i.e., $\Delta T_w < 0.1$ K), the heat transfer is controlled by natural convection near the wall surface. A constant heat transfer coefficient of $0.375\ kW/(m^2 \cdot K)$ can be deduced from published experimental data [27]. As the wall temperature increases, vapor bubbles can appear and grow, which drives the heat transfer into the nuclear boiling regime. In this regime, we adopt the most commonly used Kutateladze correlation [28]. As ΔT_w further increases, a maximum nucleate boiling heat flux q^* is achieved and the bubbles start to coalesce into a film [29]. The wall temperature T_w rises quickly during the transition to a steady film boiling. Thereafter, ΔT_w becomes an order of magnitude greater than that in nucleate boiling. For the steady film boiling regime, the widely accepted Breen-Westwater correlation [30] is used in our simulation:

$$q_{He} = B_w \Delta T_w^{5/4} \tag{12}$$

where B_w is a constant that slightly depends on surface.

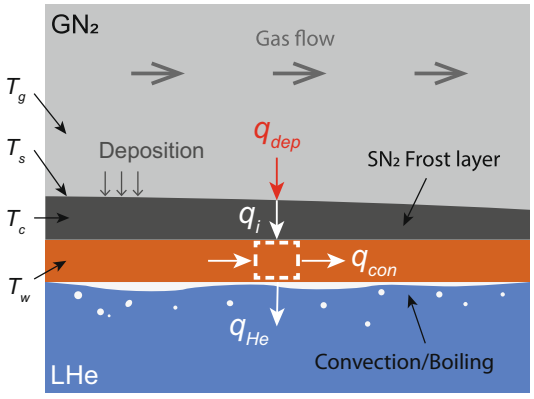

Fig. 3. Schematic showing the radial heat transfer processes through the frost layer and the tube wall.

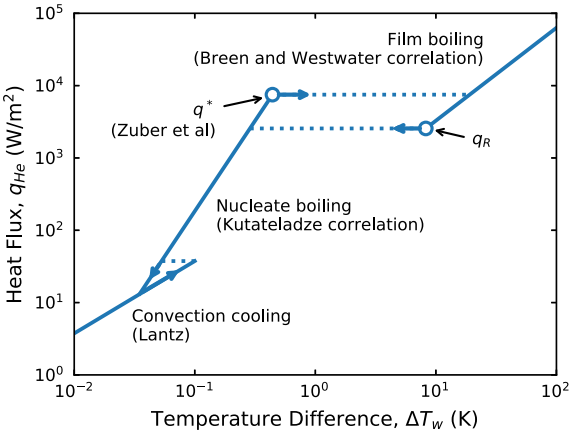

Fig. 4. Heat transfer correlations of He I adopted in our modeling.

2.3. Boundary and initial conditions

At the inlet of the tube, the GN_2 flow velocity $v(0,t)$ is assumed to be at the local speed of sound, since the flow is chocked. The mass flow rate at the inlet $\dot{m}(0,t)$ can be determined based on the measured pressure change in the buffer tank using the correlation provided in Ref. [14]. Note that the buffer tank has a finite size of 230 L. As the GN_2 flows out, the tank pressure gradually drops, and so does the mass flow rate. In our model simulations, we have incorporated this slowly time-varying mass flow rate at the tube inlet for better accuracy. Then, based on the known mass flow rate and the relation $\dot{m}(0,t) = \rho_g(0,t)v(0,t)\pi D_1^2/4$, we can calculate the inlet gas density $\rho_g(0,t)$. Taking the gas temperature $T_g(0,t) = 298$ K, the inlet pressure $P(0,t)$ can be derived using the ideal gas law. At the outlet, the copper tube used in our experiments has a closed end. Nevertheless, the measurements are usually made at short times to avoid influence of the gas reflected from the closed end [16]. In our model, we set an simple open boundary at the outlet of the tube, as shown in Fig. 1.

As for the initial conditions, we set the insulated stainless steel section of the tube to have the experimentally measured initial temperature profile [17]. The copper section of the tube immersed in the He I bath has an initial temperature of 4.2 K. To avoid potential numerical instability, we also set an infinitesimal initial gas pressure in the evacuated tube.

3. Results and discussion

We have conducted numerical simulations to solve the 1D gas dynamics equations and the radial heat transfer equations using a two-step first-order Godunov-type finite-difference method [31]. This Godunov scheme is known to be efficient and reliable in solving nonlinear hyperbolic equations [32]. The physical properties of nitrogen, copper and stainless steel used in our simulations are extracted from existing literature [33,34]. In what follows, we first present the simulation results to compare with

experimental observations for model validation. We then discuss the insights we have gained on the GN_2 dynamics in the tube and the growth of the frost layer.

3.1. Model validation

In our experiments, the propagation of the GN_2 is detected as the abrupt temperature rise by the thermometers installed along the tube wall. To compare with the experimental observations, we first present the calculated wall temperature curves at different locations along the tube, as shown in Fig. 5. These wall temperature curves exhibit some common features: the temperature initially remains at the He I bath temperature; as the GN_2 flows into the tube and condenses on the tube wall, the temperature then rises up sharply, reaching a maximum around 50 K; subsequently, the temperature slowly decreases due to the growth of the SN_2 frost layer. Furthermore, the gradually increasing separation between adjacent temperature curves suggests a slowing down of the gas propagation. All these key features agree quite well with experimental observations.

To see more clearly the agreement between the simulated and the observed GN_2 propagation, we show in Fig. 6 both the measured wall temperature curves and the calculated ones at the same thermometer locations. It is clear that these two sets of curves match fairly well except at the last thermometer location. The measured temperature by the last thermometer rises earlier than the calculated one. This is likely caused by the reflection of the shock front and the accumulation of GN_2 at the closed end in the experiment, which may effectively enhance the mass deposition at the last thermometer since it is placed close to the tube end. We would like to note that in this simulation, we have adjusted the coefficient B_w in the Breen-Westwater correlation to achieve the best match between simulation and experimental data. Nevertheless, the optimum B_w value is found to be $0.017\,W/(cm^2{\cdot}K^{5/4})$, which is close to the recommended value of $0.013\,W/(cm^2{\cdot}K^{5/4})$ by Smith for cylindrical heaters with a diameter over 1 cm [35]. This slightly larger B_w may suggest that the helical structure of our tube system could enhance the film boiling heat transfer compared to straight tubes.

Like in the experiment, we can set a threshold (i.e., 4.7 K) on the wall temperature curves to determine the "rise time" (i.e., apparent gas front arrival time), as shown in Fig. 6. The derived rise time as a function of the thermometer location is shown in Fig. 7. Again, we see an excellent agreement between the calculated and the measured results, which clearly validates the fidelity of the model simulation.

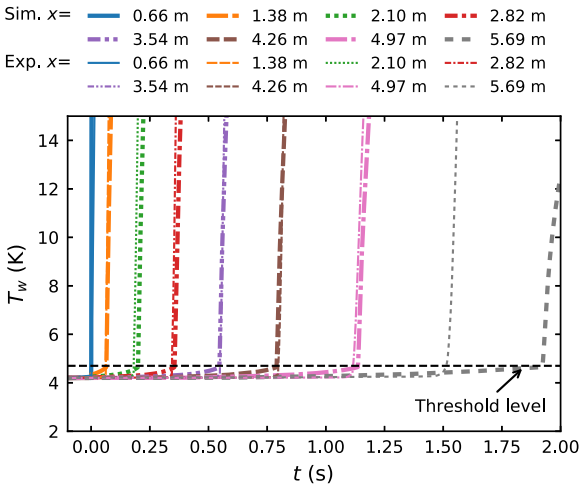

Fig. 6. Comparison of the calculated and measured wall temperature curves $T_w(t)$ at locations where the thermometers are installed.

3.2. Dynamical behavior of GN_2

We now discuss the dynamical propagation of the GN_2 in the tube. In Fig. 8, we show the simulated spatial profiles of the GN_2 density, temperature, pressure, velocity, and the wall temperature in the tube at a number of propagation times. These profiles show three distinct regions:

(1) Inlet region: In the insulated stainless steel tube section (i.e., the first 0.57 m in Fig. 8), the GN_2 flows through it rapidly and all the physical properties of the GN_2 in this tube section evolve to their inlet values within a few tens of milliseconds. Note that the gas pressure and density in this section are not constant and they slowly decrease with time due to the drop of buffer tank pressure during the discharge of N_2 gas.

(2) Mass deposition region: For a given propagation time t, the region between the condensation starting point (around $x = 0.57$ m) and the location where the wall temperature begins to spike up is the region where the N_2 deposition on the tube wall occurs predominantly. As an example, the two vertical solid lines in Fig. 8 mark roughly the boundaries of this region for a propagation time $t = 0.5$ s. This region can be further divided into two subregions: a nearly steady deposition subregion and a transition subregion. Again for the case of $t = 0.5$ s, the boundary between the two subregions is indicated by the dashed vertical line in Fig. 8. In the steady deposition subregion, the radial heat transfer

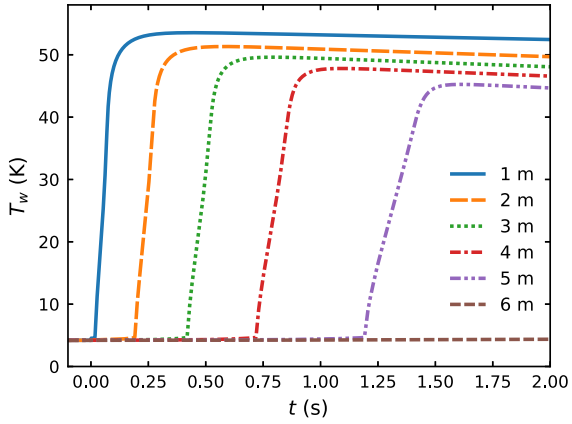

Fig. 5. Calculated wall temperature curves $T_w(t)$ at different locations along the tube.

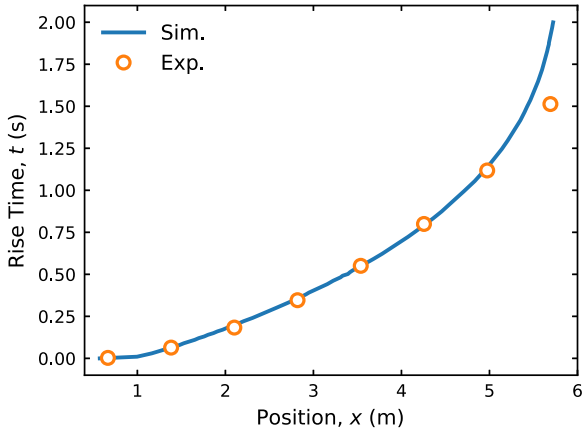

Fig. 7. Rise time of the wall temperature as a function of position along the tube.

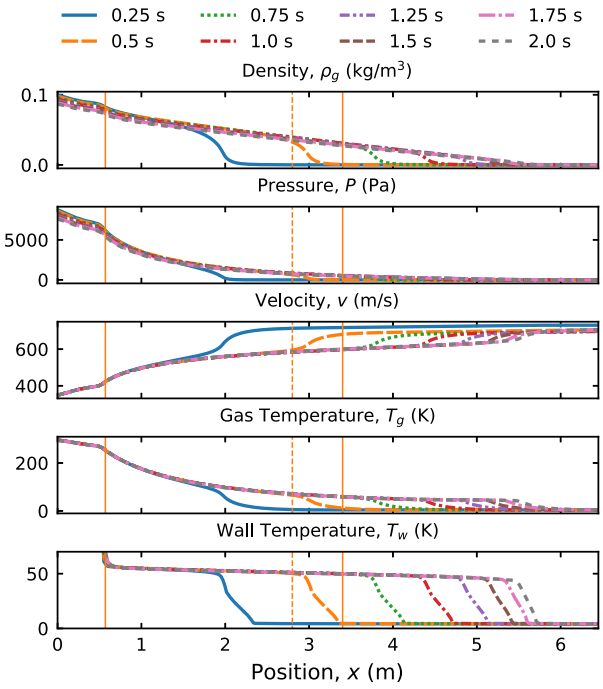

Fig. 8. Calculated spatial profiles of the N_2 density, pressure, velocity, temperature, and the wall temperature at various propagation time t. The vertical solid and dashed lines mark the boundaries of different mass deposition regions for $t = 0.5$ s, as discussed in the text.

reaches a dynamical equilibrium state. A nearly constant GN_2 mass deposition rate on the tube wall is observed, which is associated with a steady film-boiling heat transfer at a flux of about 23 kW/m^2 into the He I bath. The wall temperature changes only slightly along the tube in this subregion. Contrastingly, in the roughly 0.5 m wide transition subregion, both the GN_2 mass deposition rate and the heat transfer to the He I bath varies significantly with x. The mass deposition rate in this subregion is found to be significantly higher than that in the steady deposition subregion, which causes the rapid drop of the gas density, temperature, and pressure in this subregion, as seen in Fig. 8. The heat transfer to He I in this subregion undergoes transition from convection cooling to steady film boiling.

(3) Tail region: This region refers to the tube section beyond the mass deposition region and is featured by very low gas pressure and density. Indeed, if one looks closely in the far tail part of the GN_2 property profile curves, there exists a shock front across which there is an abrupt change of the GN_2 properties. This shock front propagates at an extremely high speed, close to the theoretical prediction of $2c_0/(\gamma - 1)$ for shock expansion in good vacuum [7]. It passes through the entire tube length in a few milliseconds and is not visible at the timescale shown in Fig. 8. Following the shock front, the gas velocity remains nearly constant at about 860 m/s in the entire tail region. But due to the low gas pressure and density in this region, there is negligible mass deposition (i.e., T_s remains at less than 4.6 K), and the heat transfer to He I is by natural convection.

3.3. Growth of the frost layer

Our model also allows us to study the growth of the SN_2 frost layer. As mentioned in Section 2.2, we have adopted the density and thermal conductivity of solid nitrogen in our model simulation. Indeed, the exact form of the frost layer highly depends on the surface temperature and mass deposition rate. In the free molecular flow regime and at low surface temperatures, the frost layer more likely takes a disordered polycrystalline structure with large voids. But at relatively high surface temperatures and large deposition rate, the increased mobility of the molecules on the solid surface can lead to the formation of a close-packed crystalline structure [36,37]. Specifically, it has been observed that for nitrogen, as the deposition rate and the surface temperature increase, the density and the thermal conductivity of the nitrogen frost layer can increase and approach the values for solid nitrogen formed from its liquid phase [36,24]. In our experiments, the wall temperature rises from 4.2 K to about 50 K within tens of milliseconds. The N_2 mass deposition largely occurs following this abrupt temperature rise. Therefore, we adopt the SN_2 property values recommended in Ref. [36] for the frost layer.

The calculated frost layer thickness as a function of time at different locations along the tube is shown in Fig. 9. The deposition starts as the front of the "mass deposition region" reaches the location of interest. Within a time period less than 100 ms, a rapid mass deposition occurs, which leads to formation of a frost layer of about 0.03 mm thick. This rapid deposition is the cause of the "transition subregion" in Fig. 8. As the wall and the frost surface temperatures rise, the mass deposition slows down and evolves into a state with a nearly constant mass deposition rate, as evidenced in Fig. 9 by the almost linear dependance of the frost layer thickness on time. This constant deposition rate reflects the nearly constant heat flux into He I in the "steady deposition subregion". Note that due to the relative high gas temperature and density near the inlet, convective heat transfer from the gas to the wall contributes a significant fraction of the heat deposition in this region. Therefore, the steady mass deposition rate near the inlet is lower than that at other locations downstream.

In Fig. 10, we show the calculated profiles of the thickness and surface temperature of the frost layer as well as the wall temperature profile at $t = 2$ s. This propagation time typically corresponds to the end of experimental measurements, since the front of the "mass deposition region" almost reaches the end of the tube. We can see that the thickness of the frost layer increases from the inlet, reaches a maximum of about 0.11 mm at around $x = 2.13$ m, then decreases gradually toward the tube end. This small thickness justifies our treatment of the temperature profile within the frost layer as discussed in Section 2.2. The temperature difference between the frost surface and the wall temperature show the same trend. A maximum temperature difference of 2.41 K is observed at $x = 2.13$ m, which is the consequence of the thermal resistance of the frost layer. Due to the insulation of the frost layer, the copper wall temperature gradually drops after reaching a maximum value as observed in our experiments [16].

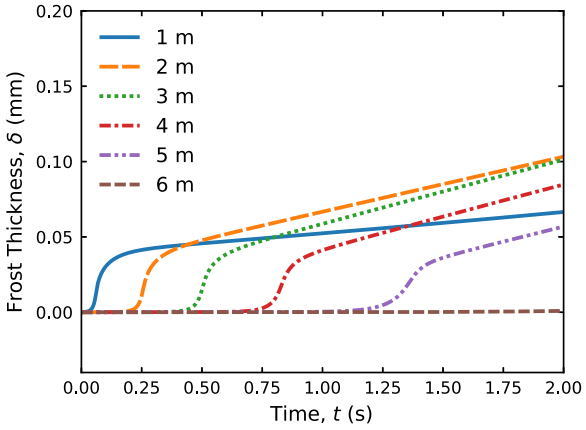

Fig. 9. Calculated frost layer thickness as a function of time at different locations along the tube.

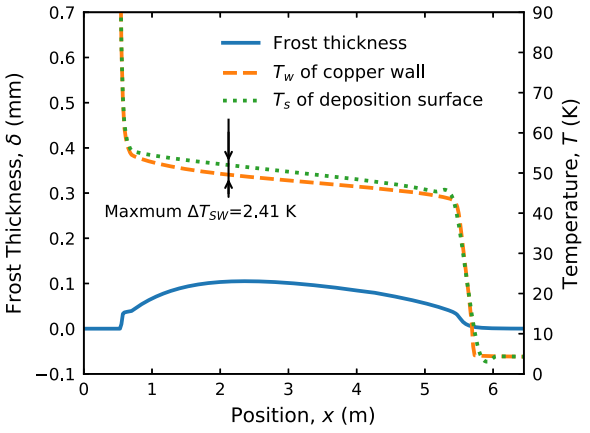

Fig. 10. Calculated profiles of the frost layer thickness, its surface temperature, and the wall temperature at $t = 2$ s.

4. Conclusion

We have presented a theoretical model that systematically accounts for the propagation and condensation of nitrogen gas in an evacuated He I cooled tube. Numerical simulations based on this model have been conducted. From these simulations, we have obtained information about the time evolution of the gas properties in the tube, the growth of the frost layer on the tube inner surface, and the wall temperature variations. The model simulation is validated by the excellent agreement between the calculated and the observed rise times of the wall temperatures at the locations where the thermometers are installed. This agreement also means that the observed exponential slowing down of the gas propagation is well reproduced.

Our simulation results also provide us some important insights into the complex heat and mass transfer processes following the vacuum beak in the cold tube. First, the apparent gas front propagation observed in the experiment indeed corresponds the propagation of the front of the "mass deposition region" that we identified in Section 3.2. Second, within the "mass deposition region", the gas deposition occurs predominantly in the "steady deposition" subregion with a nearly time independent mass deposition rate. As the gas propagates, the steady mass deposition subregion expands in length, since the other subregion (i.e., the "transition subregion") has a small and roughly constant length of about 0.5 m. Based on this observation, one can easily imagine that for a sufficiently long tube such as an accelerator beamline tube, after a certain propagation time, the mass flowing into the tube would be completely consumed by mass deposition in the steady deposition zone. Therefore, the gas propagation would appear to cease. In this situation, the length of the mass deposition region would tell us the maximum range of frost contamination in the beamline tube, which is of great practical significance.

Indeed, at low inlet mass flow rates, this interesting ceasing phenomenon can be observed even in our tube system with a limited length. We plan to present the relevant experimental and analysis results for various inlet mass flow rates and gas pressures in a future publication. We will also conduct simulations for gas propagation in the He II cooled tube. These studies will produce key knowledge for the development of safety standards for beamline cryogenic system design.

Declaration of Competing Interest

There are no conflict of interest in this work.

Acknowledgments

The authors acknowledge the support by U.S. Department of Energy under Grant No. DE-SC0020113. The work was conducted at the National High Magnetic Field Laboratory, which is supported by National Science Foundation Cooperative Agreement No. DMR-1644779 and the state of Florida. The authors would also like to thank Prof. S.W. Van Sciver for valuable discussions.

Appendix A. Supplementary material

Supplementary data associated with this article can be found, in the online version, at https://doi.org/10.1016/j.ijheatmasstransfer.2019.118883.

References

[1] S.M. Harrison, Loss of vacuum experiments on a superfluid helium vessel, IEEE Trans. Appl. Supercond. 12 (2002) 1343–1346, https://doi.org/10.1109/TASC.2002.1018651.
[2] C. Heidt, A. Henriques, M. Stamm, S. Grohmann, First experimental data of the cryogenic safety test facility PICARD, IOP Conf. Ser.: Mater. Sci. Eng. 171 (2017) 012044, https://doi.org/10.1088/1757-899X/171/1/012044.
[3] G.F. Xie, X.D. Li, R.S. Wang, Study on the heat transfer of high-vacuum-multilayer-insulation tank after sudden, catastrophic loss of insulating vacuum, Cryogenics 50 (2010) 682–687, https://doi.org/10.1016/j.cryogenics.2010.06.020.
[4] C. Heidt, S. Grohmann, M. Süßer, Modeling the pressure increase in liquid helium cryostats after failure of the insulating vacuum, in: Advances in Cryogenic Engineering: Transactions of the Cryogenic Engineering Conference, Anchorage, USA, 2014, pp. 1574–1580. https://doi.org/10.1063/1.4860894.
[5] M. Seidel, D. Trines, K. Zapfe, Failure Analysis of the Beam Vacuum in the Superconducting Cavities of the TESLA Main Linear Accelerator, Technical Report TESLA-Report 2002–06, Deutsches Elektronen Synchrotron DESY, Hamburg, Germany, 2002.
[6] M. Wiseman, K. Crawford, M. Drury, K. Jordan, J. Preble, Q. Saulter, W. Schneider, Loss of cavity vacuum experiment at CEBAF, in: Advances in Cryogenic Engineering: Transactions of the Cryogenic Engineering Conference, Boston, USA, 1994, pp. 997–1003.
[7] P. Wesseling, Principles of Computational Fluid Dynamics, number 29 in Springer Series in Computational Mathematics, first ed., Springer-Verlag, Berlin, Germany, 2001.
[8] E.F. Toro, Riemann Solvers and Numerical Methods for Fluid Dynamics: A Practical Introduction, third ed., Springer, Dordrecht, Netherlands, 2009.
[9] T. Boeckmann, D. Hoppe, K. Jensch, R. Lange, W. Maschmann, B. Petersen, T. Schnautz, Experimental tests of fault conditions during the cryogenic operation of a XFEL prototype cryomodule, in: International Cryogenic Engineering Conference 2008, Seoul, Korea, 2008.
[10] A.A. Dalesandro, J. Theilacker, S.W. Van Sciver, Experiment for transient effects of sudden catastrophic loss of vacuum on a scaled superconducting radio frequency cryomodule, in: Advances in Cryogenic Engineering: Transactions of the Cryogenic Engineering Conference, Spokane, USA, 2012, pp. 1567–1574. doi:10.1063/1.4707087.
[11] M. Ady, M. Hermann, R. Kersevan, G. Vandoni, D. Ziemianski, Leak propagation dynamics for the HIE-ISOLDE superconducting linac, in: Proceedings of the 5th International Particle Accelerator Conference, Dresden, Germany, 2014, pp. 2351–2353, https://doi.org/10.18429/jacow-ipac2014-wepme039.
[12] M. Ady, Measurement campaign of 21–25 July 2014 for evaluation of the HIE-ISOLDE inrush protection system, CERN Technical Note TE-VSC-1414574, CERN, Switzerland, 2014.
[13] R.C. Dhuley, Gas Propagation in a Liquid Helium Cooled Vacuum Tube Following a Sudden Vacuum Loss Dissertation, Florida state university, Tallahassee, USA, 2016.
[14] R.C. Dhuley, S.W. Van Sciver, Propagation of nitrogen gas in a liquid helium cooled vacuum tube following sudden vacuum loss – Part I: Experimental investigations and analytical modeling, Int. J. Heat Mass Transf. 96 (2016) 573–581, https://doi.org/10.1016/j.ijheatmasstransfer.2016.01.077.
[15] R.C. Dhuley, S.W. Van Sciver, Propagation of nitrogen gas in a liquid helium cooled vacuum tube following sudden vacuum loss – Part II: analysis of the propagation speed, Int. J. Heat Mass Transf. 98 (2016) 728–737, https://doi.org/10.1016/j.ijheatmasstransfer.2016.03.077.
[16] N. Garceau, S.R. Bao, W. Guo, Heat and mass transfer during a sudden loss of vacuum in a liquid helium cooled tube – Part I: interpretation of experimental observations, Int. J. Heat Mass Transf. 129 (2019) 1144–1150, https://doi.org/10.1016/j.ijheatmasstransfer.2018.10.053.
[17] N. Garceau, S.R. Bao, W. Guo, S.W. Van Sciver, The design and testing of a liquid helium cooled tube system for simulating sudden vacuum loss in particle accelerators, Cryogenics 100 (2019) 92–96, https://doi.org/10.1016/j.cryogenics.2019.04.012.
[18] K.M. Welch, Capture Pumping Technology, second ed., Elsevier, Amsterdam, Netherlands, 2001.

[19] R.A. Haefer, Cryogenic vacuum techniques, J. Phys. E: Sci. Instrum. 14 (1981) 273–288, https://doi.org/10.1088/0022-3735/14/3/002.
[20] N. Fray, B. Schmitt, Sublimation of ices of astrophysical interest: a bibliographic review, Planet. Space Sci. 57 (2009) 2053–2080, https://doi.org/10.1016/j.pss.2009.09.011.
[21] S. Deng, D. Cassidy, R. Greaves, A. Mills, Sticking coefficient of nitrogen on solid N2 at low temperatures, Appl. Surf. Sci. 253 (2007) 9467–9469, https://doi.org/10.1016/j.apsusc.2007.06.025.
[22] J.P. Dawson, J.D. Haygood, Cryopumping, Cryogenics 5 (1965) 57–67, https://doi.org/10.1016/S0011-2275(65)80002-9.
[23] M. Bland, The cryopumping of water vapour in the continuum pressure region, Cryogenics 15 (1975) 639–643, https://doi.org/10.1016/0011-2275(75)90094-6.
[24] G. Davey, Cryopumping in the transition and continuum pressure regions, Vacuum 26 (1976) 17–22, https://doi.org/10.1016/S0042-207X(76)80414-9.
[25] F.P. Incropera, D.P. Dewitt, T.L. Bergman, A.S. Lavine, Fundamentals of Heat and Mass Transfer, sixth ed., John Wiley & Sons, Hoboken, USA, 2007.
[26] C. Schmidt, Transient heat transfer to liquid helium and temperature measurement with a response time in the microsecond region, Appl. Phys. Lett. 32 (1978) 827–829, https://doi.org/10.1063/1.89939.
[27] J. Lantz, Heat Transfer Correlations Between a Heated Surface and Liquid Superfluid Helium Thesis, Linköpings universitet, Linköping, Sweden, 2007.
[28] S.W. Van Sciver, Helium Cryogenics, International Cryogenics Monograph Series, second ed., Springer, New York, USA, 2012.
[29] N. Zuber, M. Tribus, J. Westwater, The hydrodynamic crisis in pool boiling of saturated and subcooled liquids, in: Proceeding of 1961–62 International Heat Transfer Conference, volume 2 of International development in heat transfer, ASME, Boulder, USA, 1961, pp. 230–236.
[30] B.P. Breen, J.W. Westwater, Effect of diameter of horizontal tubes on film boiling heat transfer, Chem. Eng. Prog. 58 (1962) 67–72.
[31] I. Danaila, P. Joly, S.M. Kaber, M. Postel, An Introduction to Scientific Computing: Twelve Computational Projects Solved with MATLAB, Springer-Verlag, New York, USA, 2007.
[32] G.A. Sod, A survey of several finite difference methods for systems of nonlinear hyperbolic conservation laws, J. Comput. Phys. 27 (1978) 1–31, https://doi.org/10.1016/0021-9991(78)90023-2.
[33] K. Stephan, R. Krauss, A. Laesecke, Viscosity and thermal conductivity of nitrogen for a wide range of fluid states, J. Phys. Chem. Ref. Data 16 (1987) 993–1023, https://doi.org/10.1063/1.555798.
[34] T. Flynn, Cryogenic Engineering, second ed., Marcel Dekker, New York, USA, 2004, https://doi.org/10.1201/9780203026991.
[35] R. Smith, Review of heat transfer to helium I, Cryogenics 9 (1969) 11–19, https://doi.org/10.1016/0011-2275(69)90251-3.
[36] T. Cook, G. Davey, The density and thermal conductivity of solid nitrogen and carbon dioxide, Cryogenics 16 (1976) 363–369, https://doi.org/10.1016/0011-2275(76)90217-4.
[37] T. Scott, Solid and liquid nitrogen, Phys. Rep. 27 (1976) 89–157, https://doi.org/10.1016/0370-1573(76)90032-6.